Journal of Physics D: Applied Physics

PAPER

RECEIVED
11 October 2025

REVISED
6 February 2026

ACCEPTED FOR PUBLICATION
26 February 2026

PUBLISHED
30 March 2026

Comparison of four treatment methods for modeling streamer–to–spark discharge problems

Xiaochi Ma, Luying Bai, Yifei Zhu* and Yun Wu*

National Key Lab of Aerospace Power System and Plasma Technology, Xi'an Jiaotong University, Xi'an 710049, People's Republic of China

* Authors to whom any correspondence should be addressed.

E-mail: yifei.zhu.plasma@gmail.com and wuyun1223@126.com

Keywords: plasma simulation, spark model, semi-implicit methods, adaptive mesh refinement

Abstract

A spark is a discharge phenomenon that occurs when streamers contact each other to form discharge channels and is characterized by rapidly increasing plasma densities and amounts of energy deposited. High–density plasma generally exists throughout the discharge channel, making numerical simulations challenging, especially under conditions requiring rapid evaluation. The conventional explicit plasma–fluid model exhibits extremely low computational speeds when modeling spark discharges, whereas the widely used linear field and ambipolar diffusion models require algorithm switching. Systematic evaluations and comparative analyses of streamer–to–spark processes have not yet been reported, and issues of computational efficiency and accuracy have not yet been adequately addressed. Therefore, in this study, we (1) compared, analyzed, and summarized the limitations of the conventional explicit plasma–fluid, linear field, and ambipolar diffusion models for spark–discharge simulations and (2) integrated structured adaptive mesh refinement and semi–implicit methods into the 2D parallel plasma solver *PASSKEy* to achieve comprehensive streamer–to–spark simulations without model switching. An optimal time–step range for our code in spark modeling is proposed, and the corresponding errors are estimated.

1. Introduction

Streamer and spark discharges are essential plasma phenomena that form the basis for various emerging application–driven areas, including plasma–activated water for environmental, biomedical, and agricultural applications [1–3] and plasma–assisted nitrogen fixation for sustainable chemistry [4–7]. These applications are affected by the energy deposition and discharge channel evolution of streamers or sparks. Accordingly, developing robust and efficient numerical tools for resolving the streamer–to–spark transition is crucial for linking discharge physics with practical performance in these emerging applications.

Numerical simulations are essential for analyzing and investigating gas discharges, and the selection of the most appropriate numerical model depends on the specific discharge issues and operating conditions. In general, the widely used models for gas discharge problems include global models [8, 9], particle–in–cell (PIC) models [10], and plasma–fluid models [11, 12]. For modeling atmospheric discharges, the 0D global model is inherently limited by its lack of spatial distribution information of species, and the PIC model incurs prohibitively high computational costs for high–pressure discharges. Consequently, the plasma–fluid model, which achieves acceptable accuracy at relatively low computational costs, has become the mainstream method for streamer–to–spark discharges [13, 14]. However, the streamer–to–spark electron density can increase from an initial $10^{10}\,\mathrm{m}^{-3}$ to over $10^{22}\,\mathrm{m}^{-3}$ [15], thereby

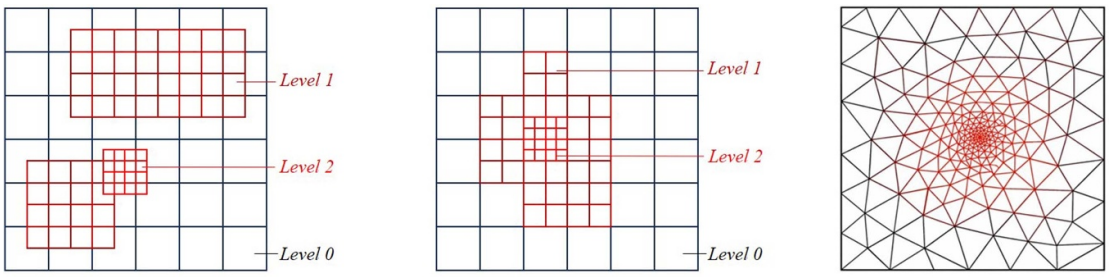

Figure 1. Schematic of three AMR strategies: (a) Block–based structured AMR, (b) cell–based structured AMR, and (c) unstructured AMR.

effectively filling the entire plasma channel. High electron densities impose constraints on the mesh size when discretizing equations spatially and restrict the permissible time step for temporal integration:

(1) Spatial limitations: The typical mesh size in the atmosphere is approximately 1 μm, considering the constraints imposed by the Debye length and plasma frequency. The electrode gap is usually greater than 1 mm, indicating a difference of four to five orders of magnitude between the mesh size and overall computational domain. If all the meshes within the entire discharge channel are prerefined, then a significant amount of computing resources is inevitably wasted. The electron sheath near the cathode is a secondary spatial influencing factor. The mesh employed in the electron sheath region should be finer than that used in the volumetric discharge region to accurately analyze the physical phenomena therein. These two factors result in a nonuniform mesh distribution and increase the computational time.

Therefore, to reduce the spatial computational costs, an adaptive mesh refinement (AMR) strategy has been applied to gas discharge modeling. Unfer *et al* [16] developed an explicit asynchronous integration scheme combined with the AMR approach (AAMR). AAMR can achieve a CPU time gain factor of $>$10 compared to the regular asynchronous scheme for equivalent precision. Teunissen and Ebert [17] investigated the plasma simulation framework Afivo, which employs a quadtree/octree AMR to solve 2D/3D streamer problems. They effectively overcame the challenges posed by the enormous number of meshes required for 3D streamer simulations. Pancheshnyi *et al* [18] examined an AMR method for modeling both negative and positive N_2 streamers. Liu [19] developed two AMR algorithms for fluid–based streamer simulations, incorporating advanced time–split integration schemes that enhanced the accuracy and efficiency of plasma discharge modeling. Niknezhad *et al* [20] used an AMR 3D plasma–airflow model to demonstrate that negative coronas are weakly affected by lateral wind, revealing the cathode–directed streamer mechanism of Trichel pulses. Lin *et al* [21] presented an efficient MPI–based 3D streamer simulator using a semi–implicit (SI) scheme and multigrid–preconditioned FGMRES solver, achieving high parallel scalability and fast convergence for large–scale plasma discharge simulations. According to these previous studies, numerical tests indicate that the use of AMR accelerates computations by 4–5 times in 2D cases and by up to 8–12 times in 3D cases.

However, the reported speedups and robustness depend on the underlying refinement strategy and its coupling with Poisson/transport solvers, which motivates the following brief classification of the AMR strategies used in discharge simulations. Notably, AMR originated from nested mesh ideas across levels and has evolved into many variants that differ mainly in how refined meshes are generated, stored, and updated. From the perspective of mesh generation, existing AMR strategies used in discharge problems can be broadly categorized into three representative classes, as shown in figure 1: (a) block–based structured AMR [22, 23], in which the computational domain is covered by a hierarchy of blocks, and refinement is performed by replacing a parent block with a set of finer children blocks; (b) cell–based structured AMR [18, 24–29], where refinement is realized by recursive division and neighboring–level constraints are typically enforced to maintain a smooth adaptive structure; (c) unstructured AMR [30–33], which often refines nodes instead meshes to offer geometric flexibility at the cost of more complex data management.

From an algorithmic viewpoint, these studies illustrate that the performance gain of AMR depends not only on the refinement criteria but also on the underlying mesh–generation mechanism and its coupling with Poisson/transport solvers. For example, unstructured adaptive meshing offers additional flexibility through element–based refinement and mesh–quality operations, which can be advantageous for complex electrode geometries, but typically increases implementation complexity. Block–structured AMR frameworks emphasize the automated management of a tree of structured submeshes, interblock

communications, and conservative treatments at the refinement interfaces. Quadtree/octree frameworks, such as Afivo, provide a high–efficiency hierarchy and are well–suited for frequent re–gridding in streamer simulations. Cell–based AMR refines the mesh by directly applying adaptation operations to individual cells, which can closely follow highly localized gradients. This approach typically leads to more irregular refinement patterns; therefore, the simulation must update neighbor connectivity more frequently and carefully treat the flux and Poisson coupling across the coarse–fine interfaces.

Motivated by the above studies, we adopted a cell–based structured AMR strategy to efficiently solve streamer–to–spark simulations. The cell–based structured AMR was selected owing to its (a) simple and modular data structure, which enabled easy implementation of the conservative flux discretization scheme, and (b) compatibility with immersed boundary formulations, which enabled the processing of complex electrode geometries while retaining a finite volume structure. (c) The cell–based adaptation provided localized refinement near sharp gradients and evolving discharge channels, which helped reduce the number of cells and interfaces.

(2) Temporal limitations: The dielectric relaxation time constitutes a vital constraint on the time steps in spark simulations, particularly when the electron density exceeds $10^{22}\,\mathrm{m}^{-3}$. If the dielectric relaxation time, Δt_{Diel}, is assumed to be approximately $10^{-14}\,\mathrm{s}$ and the total discharge time is of the order of $10^{-8}\,\mathrm{s}$, then a temporal difference spanning six orders of magnitude exists. Various methods have been proposed to mitigate these constraints.

The linear field model [34] is frequently employed to accelerate spark–discharge simulations. In this approach, 'freezing' the electric field distribution implies that Poisson's equation and the constraints imposed by the dielectric relaxation time no longer require solving. The limitation of the linear field model lies in its inability to capture the local electric field distortions in spark discharges. When the needle tip curvature is small, lateral discharge features near the tip are often observed, which have been repeatedly reported in previous experiments and simulations [34–37]. If a constant electric field is maintained after breakdown, and subsequently, it scales linearly with the applied voltage, then an unrealistically large field may manifest near the cathode. In practice, such lateral field enhancement can be influenced by space–charge distributions, which cannot be adequately considered by linear field approximation.

The ambipolar diffusion model [38] is another viable method of simulating spark discharges. This approach was successfully applied to simulate gliding arc discharges [39–41]. An SI treatment for Poisson's equation was used in the streamer simulations. Ventzek *et al* [42] investigated an SI implementation, achieving time steps that were 10–100 times longer than the dielectric relaxation time. Kushner [43] provided a comprehensive discussion of this approach.

Moreover, the constraint imposed by the Courant–Friedrichs–Lewy (CFL) condition is a critical factor and cannot be overlooked. When employing explicit time integration schemes, the time step in each mesh must satisfy the CFL condition [44] to ensure simulation robustness. Implicit and SI treatments of transport fluxes are among the most common methods used to mitigate the limitations imposed by the CFL conditions. Lin *et al* [45] developed a 2D SI numerical program. Their code can reduce the computational time by up to 2–3 orders of magnitude, as validated by a dielectric barrier discharge benchmark. Li *et al* [46] investigated a multi–time–step explicit Euler scheme for simulating capacitive coupled discharges, which reduced the computational cost associated with the electron equations by 50%. Dung *et al* [47] proposed an implicit algorithm to accelerate 2D corona discharge simulations. This algorithm was validated using experimental results.

Although time acceleration algorithms have been developed for various discharge modes, systematic and comprehensive evaluations of the entire process of streamer–spark discharge have not yet been reported. Furthermore, the feasibility of applying the SI method for solving Poisson's equation to spark discharges has not yet been explored. Therefore, in this study, we investigated four different numerical methods to model streamer–spark discharges: the conventional explicit, linear field, ambipolar diffusion, and SI time integration with AMR methods.

In section 2, the conventional explicit plasma–fluid model used in the *PASSKEy* code is briefly introduced. Section 3 describes the different methods for modeling the streamer–to–spark discharge, including the integration of the SI method and AMR into the 2D parallel plasma solver *PASSKEy* to address the spatial and temporal constraints in streamer–to–spark discharge modeling. Section 4 presents a pin–to–pin discharge simulation performed using the conventional explicit plasma–fluid, linear field, ambipolar, and the proposed models. The characteristics and shortcomings of these models are analyzed and compared. Finally, optimal time step ranges for the *PASSKEy* framework are proposed, accompanied by an evaluation of error estimates, and a summary is provided in section 5.

2. Numerical model description

In this study, the *PASSKEy* code was used to model discharge problems. The original *PASSKEy* code is based on a fixed Cartesian mesh and the finite volume method (FVM), and it solves nanosecond pulsed discharges by coupling the electric field with plasma transport equations [48, 49]. This section introduces the basic framework of *PASSKEy*.

Based on this framework, we developed a new version of *PASSKEy* by integrating a structured AMR module and adopting SI time integration for the continuity equations to improve the robustness and efficiency of the full streamer–to–spark simulations (called the AMR model). The implementation details of the SI–AMR version of *PASSKEy* are presented in section 3.2.

2.1. Governing equations

2.1.1. Plasma continuity equations

The continuity equations of the plasma species include the drift—diffusion reaction equations for solving the species densities, and the set of drift—diffusion reaction equations can be written as

$$\frac{\partial n_i}{\partial t} + \nabla \cdot \mathbf{\Gamma}_i = S_i + S_{\mathrm{ph}},\ i = 1, 2, \ldots, N_{\mathrm{total}}, \tag{1}$$

where n_i is the number density of species i, t is the time, S_i is the reaction source term of species i, S_{ph} is the photoionization source term, $\mathbf{\Gamma}_i$ is the plasma component flux caused by the drift–diffusion approximation, which is expressed as

$$\mathbf{\Gamma}_i = \left(q_i / |q_i|\right) \mu_i n_i \boldsymbol{E} - D_i \nabla n_i, i = 1, 2, \ldots, N_{\mathrm{charge}}, \tag{2}$$

where q_i is the charge number of species i, D_i is the diffusion coefficient, μ_i is the mobility of species i, and N_{charge} is the number of charged species. $\boldsymbol{E}$ denotes the electric field.

The reaction source term S_i reflects the changes caused by the plasma reactions. S_i uses a set of ordinary differential equations to describe

$$\frac{\mathrm{d}n_i}{\mathrm{d}t} = S_i = \sum_{j=1}^{j_{\max}} Q_{ij},\ j = 1, 2, 3, \ldots, j_{\max},\ i = 1, 2, 3, \ldots, N_{\mathrm{total}}, \tag{3}$$

where j denotes the number of reactions, i is the number of species, and Q_{ij} is the source term of species i from reaction j.

$$Q_{ij} = k_j \cdot n_a \cdot n_b \cdot \ldots, \tag{4}$$

where k_j is the rate coefficient of reaction j, n_a and n_b are the density products of all reactants.

The diffusion coefficient, mobility, and reaction rates of the electrons were calculated using BOLSIG+ [50] and saved as functions of the reduced electric field E/N; in other words, the local field approximation was adopted, and the electron temperature was directly determined using E/N. For electrically neutral species, the drift–diffusion flux was neglected by restricting the transport dynamics and solving the reaction kinetics. This simplification is justified by the consideration: neutral species remain unaffected by field–driven transport owing to their zero net charge.

The photoionization source term S_{ph} reflects the ionization caused by extreme ultraviolet (EUV) radiation. The three–exponential Helmholtz model, previously suggested for quantifying the photoionization source term, is denoted as S_{ph}:

$$S_{\mathrm{ph}}\left(\vec{r}\right) = \sum_j S_{\mathrm{ph}}^j\left(\vec{r}\right),\ j = 1, 2, 3. \tag{5}$$

and S_{ph}^j can be solved using the Helmholtz equation

$$\nabla^2 S_{\mathrm{ph}}^j\left(\vec{r}\right) - \left(\lambda_j p\right)^2 S_{\mathrm{ph}}^j\left(\vec{r}\right) = -A_j p^2 I_0\left(\vec{r}\right), \tag{6}$$

where λ_j and $A_j\,(j=1,2,3)$ are the fitting parameters for the equation, p is the gas pressure, $I_0\,(\vec{r})$ is the ionization source rate. The values of λ_j and A_j can be obtained by fitting the pressure–reduced photoionization rate function ψ_0/p. The expression for ψ_0/p is obtained from the work of Pancheshnyi [51].

$$\frac{\psi_0}{p} = (pr)\sum_j A_j \mathrm{e}^{-\lambda_j pr},\ j=1,2,3, \tag{7}$$

$$\frac{\psi_0}{p} = \frac{p_q}{p+p_q}\frac{1}{4\pi}\frac{\omega}{\alpha_{\mathrm{eff}}}\frac{\int_{\lambda_{\min}}^{\lambda_{\max}} \xi_\lambda \left(\frac{\mu_\lambda}{p}\right) \mathrm{e}^{-\left(\frac{\mu_\lambda}{p}\right)pr} I_\lambda^0 \mathrm{d}\lambda}{\int_{\lambda_{\min}}^{\lambda_{\max}} I_\lambda^0 \mathrm{d}\lambda}, \tag{8}$$

$$\xi_\lambda = \frac{\sigma_{\mathrm{ionization}}\,(\lambda)}{\sigma_{\mathrm{absoption}}\,(\lambda)}, \tag{9}$$

$$\frac{\mu_\lambda}{p} = \frac{\sigma_{\mathrm{absoption}}\,(\lambda)}{k_b T}, \tag{10}$$

where pq is the quenching pressure of the emitting gas, ω is the excitation coefficient of the emitting states, α_{eff} is the effective Townsend coefficient, $(\lambda_{\min},\lambda_{\max})$ is the spectral range of the radiation, ξ_λ and μ_λ are the spectrally resolved photoionization yield and absorption coefficient, respectively, and I_λ^0 is the spectral density of the In this study, the photoionization parameters were derived from [52] and calculated using PHOTOPiC [53].

Notably, photoionization predominantly governs the positive streamer propagation. Following spark channel formation, the ionization rate undergoes significant modifications compared with the rate in the streamer–dominated regime, and photoionization ceases to drive discharge propagation. In the post–breakdown stage, the initial model assumption of substituting the production rates of EUV–generating excited species with equivalent electron source terms becomes physically invalid. Consequently, the photoionization source term is systematically deactivated during spark–discharge computations to maintain model fidelity.

2.1.2. Poisson's equation for electric field

Poisson's equation for the electric field is solved for the entire nonmetal computational domain:

$$\nabla\left(\varepsilon_0\varepsilon_{\mathrm{r}}\left(-\nabla\Phi\right)\right) = -\rho_{\mathrm{c}}, \tag{11}$$

$$\boldsymbol{E} = -\nabla\Phi, \tag{12}$$

$$\rho = \sum_{i=1}^{N_{\mathrm{charge}}} n_i q_i, \tag{13}$$

$$\frac{\partial\rho_{\mathrm{c}}}{\partial t} = \sum_{i=1}^{N_{\mathrm{charge}}} q_i\left(-\nabla\cdot\boldsymbol{\Gamma}_i\right), \tag{14}$$

where ε_0 is the vacuum permittivity, ε_{r} is the relative permittivity, Φ is the potential, $\boldsymbol{E}$ is the electric field, ρ_{c} is the space–charge density, and N_{charge} is the number of charged species.

2.1.3. Fluid equations for gas response

The fluid dynamic response of the discharge is considered to validate the *PASSKEy* code. Fluid equations (mass, momentum, and energy conservation equations) are solved for fluid variables, such as mass density, pressure, temperature, and velocities, which are compared with a benchmark.

$$\frac{\partial\rho}{\partial t} + \nabla\cdot(\rho\mathbf{u}) = 0, \tag{15}$$

$$\frac{\partial\rho\mathbf{u}}{\partial t} + \nabla\cdot(\rho\mathbf{u}\otimes\mathbf{u}) = -\nabla p + \nabla\cdot\tau + \mathbf{E}q, \tag{16}$$

$$\frac{\partial\rho e}{\partial t} + \nabla\cdot(\rho e\cdot\mathbf{u}) = -p\nabla\cdot\mathbf{u} + \nabla\cdot(k\nabla T) + \tau:\mathbf{u} + S_{\mathrm{heat}}, \tag{17}$$

Table 1. Boundary conditions of continuity equations in the *PASSKEy* code.

Boundary and flux direction	Electron	Negative ions	Positive ions
Anode, flow in	$\nabla n = 0$	$\nabla n = 0$	0
Anode, flow out	0	0	$\nabla n = 0$
Cathode, flow in	0	0	$\nabla n = 0$
Cathode, flow out	$\nabla n = 0$	$\nabla n = 0$	0
Domain boundary	$\nabla n = 0$	$\nabla n = 0$	$\nabla n = 0$

where ρ is the mass density, $\mathbf{u}$ is the gas velocity, p is the pressure, τ is the shearing stress tensor, e is the gas energy, k is the thermal conductivity determined by Sutherland's law, and T is the gas temperature.

The gas pressure p and temperature T are determined using the ideal gas equation

$$p = (\gamma - 1)\,\rho\left(e - \frac{1}{2}\mathbf{u}^2\right), \tag{18}$$

$$h = e + \frac{p}{\rho} = C_{\mathrm{p}} T, \tag{19}$$

where h is the enthalpy, C_{p} is the constant–pressure specific heat capacity of air, which is given by the following expression:

$$C_{\mathrm{p}} = \frac{\gamma}{\gamma - 1} \cdot R_{\mathrm{gas}} \cdot \frac{\Sigma n_i}{\Sigma\left(n_i \cdot M_i\right)}, \tag{20}$$

where M_i is the molar mass of the species i.

The coupling term from plasma to fluid is reflected in the body force, which influences the momentum equation. The term $\boldsymbol{F}_{\mathrm{EHD}} = \boldsymbol{E}q$ is the electrodynamic force owing to net charges, and the other coupling term is the heating source S_{heat} from plasma chemistry:

$$S_{\mathrm{heat}} = \sum_{k=1}^{k_{\max}} \left(R_k \cdot \Delta H_k\right), k = 1, 2, 3, \ldots, N_{\mathrm{react}}, \tag{21}$$

where R_k is the rate of reaction k and ΔH_k is the enthalpy of reaction k.

The coupling term from the fluid flow to the plasma is the plasma convection flux caused by the fluid flow, which is added to the continuity equation for each species.

$$\boldsymbol{\Gamma}_{i,\mathrm{conv}} = \nabla \cdot \left(\boldsymbol{u} n_i\right), i = 1, 2, \ldots, N_{\mathrm{total}}. \tag{22}$$

2.2. Boundary conditions

Different studies [54, 55] and software packages [56, 57] considered different boundaries in the plasma continuity equations. In table 1, we have summarized the boundary conditions of the *PASSKEy* code. In the case of a pin–to–pin discharge configuration, when the streamer finally penetrates the gap and forms a conductive channel, the electrons emitted by the cathode cannot be accurately predicted from a fixed secondary emission coefficient. Thus, a Neumann condition is set [58]; otherwise, the calculation crashes [37].

For Poisson's equation, the classical Dirichlet boundary condition was used at the interface between the electrodes and gas:

$$\Phi = U(t) \tag{23}$$

where $U(t)$ is the applied voltage.

To avoid the serration of the electrode boundaries caused by Cartesian mesh generation, the immersed boundary method [59] was used in Poisson's equation. Detailed implementations can be found in our previous study [60]. The Nuemann boundary conditions were written for the nonmetal boundaries.

For the fluid equations, the boundary condition settings in [61]. Briefly, a no–slip wall boundary condition was applied to the solid surfaces (electrodes), and the mass density and pressure in the ghost cells were determined through linear extrapolation from the adjacent interior cells. The velocity components were assigned opposite values in the ghost cells to enforce a zero velocity at the physical boundary. At the outlet boundary, a far–field pressure condition was imposed, and the mass density and velocity components were interpolated from the internal variables using characteristic–based reconstruction.

3. Numerical treatments for spark modeling

3.1. 'Conventional' approaches: explicit, linear field, and ambipolar diffusion models

In this section, 'traditional models' refers to the three existing approaches considered in this study, i.e. the explicit plasma–fluid, linear field model, and ambipolar diffusion models, which are discussed for comparison with the SI–AMR version of *PASSKEy* code introduced in the next section.

(1) Conventional explicit plasma–fluid model.

The conventional explicit plasma–fluid mode adopts explicit time integration. Therefore, based on the CFL conditions, the stability of the numerical solutions is determined by the time step, ranging from 10^{-5} ns to 10^{-3} ns determined by the mesh size, electron density, and electric field:

$$\Delta t_{\text{drift}} = \text{CFL}_{\text{drift}} \frac{h}{\mu_e \cdot \max\left(E_x, E_y\right)} \tag{24}$$

$$\Delta t_{\text{diff}} = \text{CFL}_{\text{diff}} \frac{h^2}{D_e} \tag{25}$$

where h is the mesh size and E_x and E_y are the electric field components in x and y directions, respectively. $\text{CFL}_{\text{drift}}$ and CFL_{diff} are the dimensionless CFL numbers for the electron drift and diffusion, respectively, and their values are both 0.1, unless otherwise specified. μ_e and D_e are the electron mobility and diffusion coefficients, respectively.

The explicit time scheme facilitates accurate computation of the nanosecond discharge but may suffer from huge computational time in the case of long–time scale spark discharges.

(2) Linear field model.

The linear field model assumes that the electric field distribution is 'frozen' and that the electric field value evolves proportionally to the applied voltage during the spark phase:

$$|\boldsymbol{E}(t)| = A \cdot U(t) \tag{26}$$

where $|\boldsymbol{E}(t)|$ is the norm of the electric field, and A is a ratio constant. When the linear field model is applied, the net flux entering and leaving each plasma mesh is assumed to be zero; that is, the drift–diffusion fluxes of the charged species are neglected, and the electron density is solely determined by the reaction source term S_i.

(3) The ambipolar diffusion model.

The ambipolar diffusion model solves the ambipolar diffusion field to calculate plasma drift–diffusion flux. The ambipolar diffusion field $\boldsymbol{E}_{\text{amb}}$ was derived based on the following quasi–neutrality assumption:

$$\boldsymbol{\Gamma}_i = -sgn\left(q_i\right)\mu_i n_i \mathbf{E}_{\text{amb}} - D_i \nabla n_i, i = 1, 2, 3, \ldots, N_{\text{char}} \tag{27}$$

$$\mathbf{E}_{\text{amb}} = \frac{\sum\limits_i sgn\left(q_i\right) D_i \nabla n_i}{\sum\limits_i \mu_i n_i}, i = 1, 2, 3, \ldots, N_{\text{char}} \tag{28}$$

The Laplace field $\boldsymbol{E}_{\text{Lapl}}$ was solved in the ambipolar model to calculate the chemical reaction rate coefficients and plasma transport parameters obtained from the current conservation equation

$$\nabla \cdot \left(\sigma\left(-\nabla\phi\right)\right) = 0 \tag{29}$$

$$\mathbf{E}_{\text{Lapl}} = -\nabla\phi, \tag{30}$$

where σ is the electrical conductivity, and e is the elementary charge. The conductivity is given by the following formula:

$$\sigma = e\sum_i \mu_i n_i. \tag{31}$$

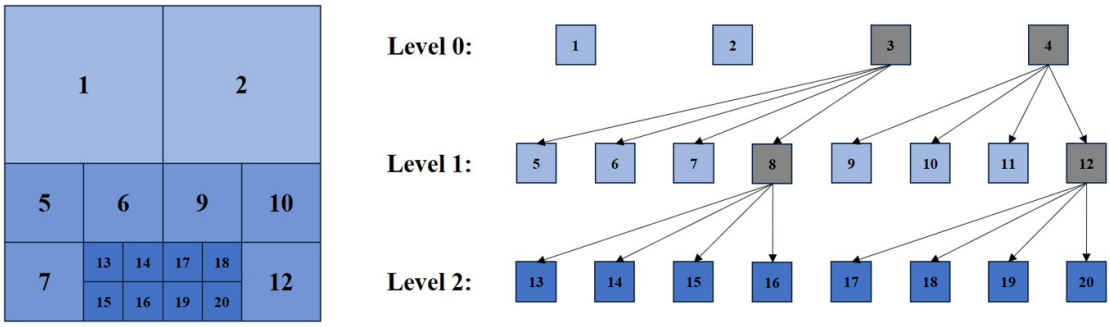

Figure 2. Schematic of adaptive mesh segmentation used in the code based on quadtree (taking three–level meshes as an example). The blue meshes with varying shades represent different levels of the active mesh in the structured AMR, and the gray square represents the refined mesh.

We found significant differences in the electron densities between the interior and exterior of the plasma channel (ranging from $10^{23}\,\mathrm{m}^{-3}$ to $10^{10}\ \mathrm{m}^{-3}$), resulting in a large spatial difference in the electric conductivity (ranging from $1.0\ \mathrm{S\,m}^{-1}$ to $10^{-12}\ \mathrm{S\,m}^{-1}$). The conductivity is too low in the region outside the spark, which can easily lead to calculation collapse. Therefore, we set the minimum conductivity to $10^{-3}\ \mathrm{S\,m}^{-1}$, ensuring computational robustness while preserving the self–consistent conductivity within the discharge channel.

3.2. SI time integration with AMR for spark discharge

As discussed in section 3.1, both the linear field and ambipolar diffusion models for spark discharges were designed to alleviate the increased computational cost associated with flux evaluations and the severely reduced time step caused by the rapid growth of electron density. However, in practical simulations, switching of physical models is often unavoidable. To address these issues without changing the governing equations, we developed an SI–AMR model using our in–house code, *PASSKEy*.

This model, hereafter referred to as 'SI–AMR model' or 'the SI–AMR version of *PASSKEy*,' combines (1) an SI time integration scheme and (2) structured AMR, to reduce the number of mesh cells and flux interfaces involved in solving Poisson's equation and the species balance equations, and relaxing the constraints imposed by the dielectric relaxation time and the electron transport time scales.

The SI–AMR version of *PASSKEy* shares the same numerical scheme as the original version. Every parent mesh has four child meshes; thus, the newly created fine meshes (child meshes) share the same information of electric field, species density, temperature, etc from the parent mesh, whereas the data in the coarse mesh are averaged from its child meshes. A base and uniform mesh is generated at initialization and then automatically refined according to the geometric shape. The meshes are then graded and refined or coarsened every 10 computing steps during the time integration, according to the predefined criteria (equation (32)) following the parent–child quadtree data structure (shown in figure 2).

$$h = h_{\max} \times \frac{1}{2^n} \leqslant \max\left(\frac{\log_{10}(n_e)}{18} h_{\min} + \frac{18 - \log_{10}(n_e)}{18} h_{\max}, h_{\min}\right), \tag{32}$$

where h is the mesh size, n is the number of refinements, n_e is the electron density, $h_{\min}$ and $h_{\max}$ are the predefined minimum and maximum mesh sizes, respectively, as defined by the user. Thus, any grid size is continuously refined from the maximum grid size, with each refinement being half of the original grid size. The number of refinements is calculated using equation (32), which is related to the electron density. In particular, when the electron density is greater than $1.0 \times 10^{18}\,\mathrm{m}^{-3}$, the mesh size is uniformly refined to the smallest size $h_{\min}$.

The flowchart is shown in figure 3, and the AMR workflow consists of four key steps.

Step 1: Evaluation of the mesh tagging and target size. We looped over all the meshes and computed the target mesh size using equation (32). Then, each mesh was tagged for refinement or coarsening by comparing its current size with the target size. The meshes with mismatched sizes were marked.

Step 2: Mesh refinement (or coarsening). All the tagged meshes were refined or coarsened based on a quadtree hierarchy. Refinement splits a parent mesh into four children, whereas coarsening merges eligible children back into their parents. This process was repeated until the mesh size satisfied the target size requirement.

Step 3: Mesh fixing. After refinement (or coarsening), a patching step was applied to smooth the mesh size transitions. Specifically, for each refined or coarsened mesh, we inspected its four orthogonal

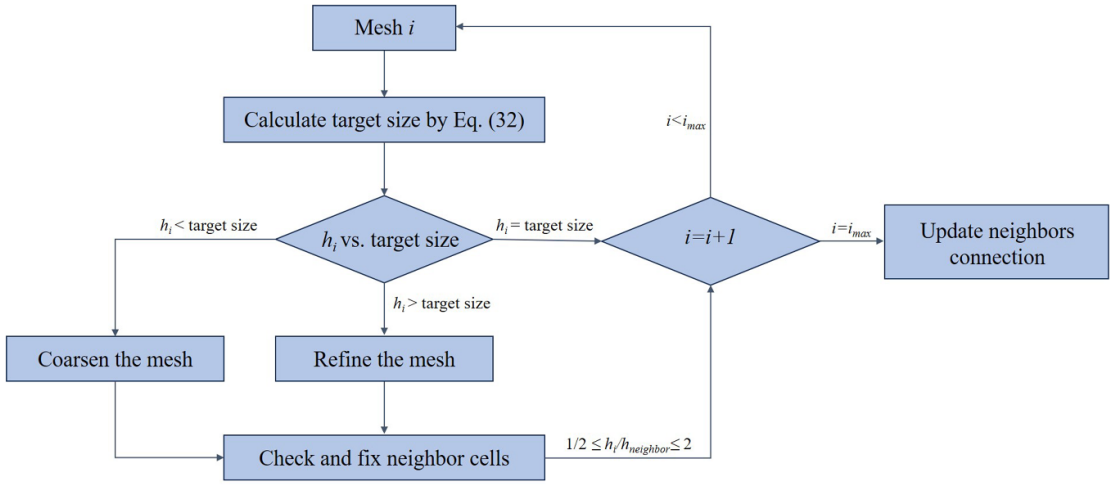

Figure 3. Workflow of the quadtree structured AMR procedure. i is the mesh index and h_i is the mesh size of index i.

neighbors (up/down/left/right) and four diagonal neighbors. If the size difference between a mesh and any neighbor exceeded by a factor of 2.0 (equivalently, their refinement levels differed by more than one), then the neighboring mesh was further refined such that the adjacent meshes differed by at most one refinement level.

Step 4: Update neighbor connections. Because refinement (or coarsening) created new (or replaced old) meshes, we rebuilt the neighbor connectivity, including adjacency pointers and indices, to ensure self–consistent flux evaluation, discretization, and boundary processing.

The discretization of the equations is still based on the FVM. *PASSKEy* code refers to previously well–established publications [45, 62, 63], employs SI discretization schemes for the Poisson's equation and the species transport equations.

In short, SI treatments change the solution time of Poisson's equation from t to $t+\Delta t$. The SI Poisson solver was implemented and validated using the original PASSKEy code, as follows:

$$\nabla \cdot \left(\varepsilon_0 \varepsilon_{\mathrm{r}} (-\nabla \phi)^{t+\Delta t}\right) = {\rho_{\mathrm{c}}}^{t+\Delta t} \tag{33}$$

$${\rho_{\mathrm{c}}}^{t+\Delta t} = {\rho_{\mathrm{c}}}^{t} + \Delta t \frac{\partial \rho_{\mathrm{c}}}{\partial t}. \tag{34}$$

The partial derivative of the space charge over time can be expressed as:

$$\frac{\partial \rho_{\mathrm{c}}}{\partial t} = \sum_i \left[-\nabla \cdot \left(|q_i| \, {\mu_i}^t {n_i}^t \mathbf{E}^{t+\Delta t} - q_i {D_i}^t \nabla {n_i}^t\right)\right]. \tag{35}$$

The SI Poisson's equation can predict the space charge at the next time instant and can be solved independently before the species continuity equations, which has been proven to be an important method for releasing the constraint of the dielectric relaxation time (equation (36)). High electron densities in spark discharges are expected to significantly reduce the dielectric relaxation time; if we assume $n_{\mathrm{e}} \simeq 5.0 \times 10^{22}\, m{-}3$, $\mu_{\mathrm{e}} \simeq 5.0 \times 10^{-1}\, m^2\, Vs^{-1}$, then the estimated dielectric relaxation time Δt_{Diel} is 1.11×10^{-14} s. Considering that the characteristic timescale of spark discharges is $10^{-8}\,\mathrm{s} \sim 10^{-6}\,\mathrm{s}$, a time difference of 6–8 orders of magnitude is observed.

$$\Delta t_{\mathrm{Diel}} = \frac{\varepsilon_0}{e \cdot \mu_{\mathrm{e}} \cdot n_{\mathrm{e}}} \tag{36}$$

where ϵ_0 is vacuum permittivity, e is elementary charge, μ_{e} is electron mobility, n_{e} is electron density.

The SI treatment for species balance equations is referred to in [45]. The partial differential equations are converted into matrices instead of using algebraic operations.

$${n_i}^{t+\Delta t} = {n_i}^t - \Delta t \nabla \cdot \left(\mathrm{sgn}\,(q_i)\, {\mu_i}^t {n_i}^{t+\Delta t} \mathbf{E}^{t+\Delta t} - {D_i}^t \nabla {n_i}^{t+\Delta t}\right), i = 1, 2, 3, \ldots, N_{\mathrm{char}}. \tag{37}$$

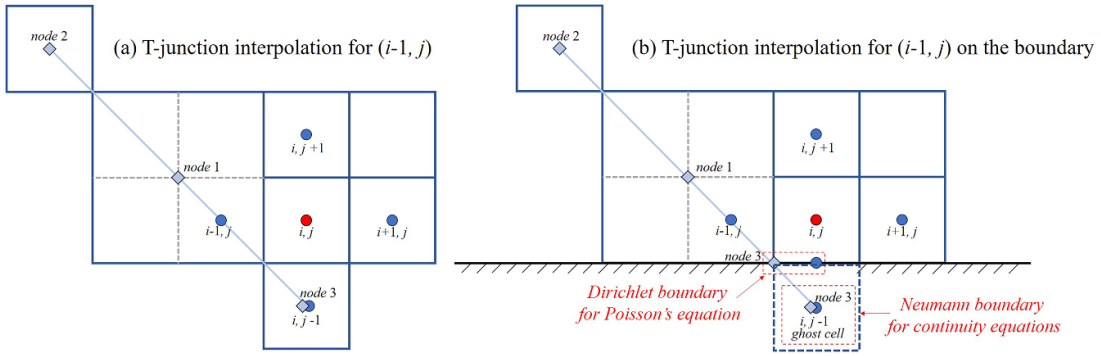

Figure 4. Diagonal interpolation scheme for stencils of Poisson's equation at the T–junction (a) in the computational domain and (b) on the boundary. Nodes 1, 2, and 3 are used to interpolate node (i-1, j), and the dashed mesh is the ghost boundary cell of the continuity equations.

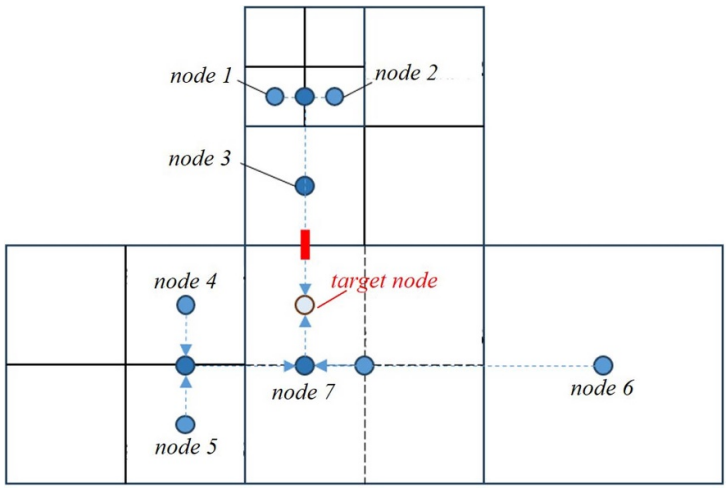

Figure 5. Traditional interpolation scheme for stencils of Poisson's equation at the T–junction.

Notably, special treatment is required at the interfaces between the coarse and refined meshes (called T–junctions). To ensure second–order accuracy of Poisson's equation and continuity equations at the T–junctions (refined–coarsened interface), a novel stencil construction technique based on diagonal interpolation was used [64], and the species density in the buffer meshes at the T–junctions was updated based on the diagonal interpolation scheme (figure 4).

Figure 4 illustrates the discretization scheme, in which the red spheres represent unsolved nodes (i.e. mesh points requiring a solution), and the blue spheres denote the four nearest neighbors in the north, south, east, and west directions. These five–point stencils constitute the fundamental elements of the spatial discretization. At the interfaces between refined and coarse meshes, buffer cells, such as cells (i-1, j), require spatial interpolation, as indicated by the light–blue diamond markers. Specifically, the electrical potential and species density at (i-1, j) are reconstructed via bilinear interpolation from four surrounding coarse–mesh quadrature points (marked as node 1 to node 3 in the subplot). This method is more efficient than the traditional interpolation stencil (see figure 5), which requires seven nodes for interpolating the target node value.

The streamer–spark modeling methods employed in this study are summarized and compared in table 2. Evidently, the conventional explicit plasma–fluid and SI–AMR models do not require switching between the models. In both the linear field and ambipolar diffusion models, the computational algorithms for the electric field and transport flux calculations are modified. A comparison of the results obtained using the four models is presented in section 4.1.

Table 2. Summary of the features of the streamer–spark modeling methods.

Models	Electric field solver		Transport flux scheme	
	Streamer	Spark	Streamer	Spark
Classic model	Poisson's equation		Scharfetter–Gummel (SG) scheme (explicit)	
Linear field model	Poisson's equation	'Frozen' electric field	SG scheme, (explicit)	No transport flux
Ambipolar diffusion model	Poisson's equation	Laplace field	SG scheme, (explicit)	Ambipolar diffusion flux
SI–AMR model	Poisson's equation		SG scheme (semi–implicit)	

Table 3. Model settings of pin–to–pin discharge.

Model Setup	Value
Geometry (the shape of electrodes)	Hyperbola, the curve expression is: $\frac{y^2}{0.00125^2} - \frac{x^2}{0.00061237^2} = 1$
Background gas temperature	1000 K
Background pressure	1.0 atm
Initial electron density	$1.0 \times 10^{10}\,\mathrm{m}^{-3}$
Input voltage	$0 \sim 5100\mathrm{V},\ 10\,\mathrm{ns}$ pulse
Computation time	10 ns
Minimal mesh size ($h_{\min}$)	2 μm
Electrode gap distance	2.5 mm
Spark model	The spark model is open when $n_{e,\max} = 1.0 \times 10^{22}\,\mathrm{m}^{-3}$.

4. Results and discussions

4.1. Benchmark: pin–to–pin discharges

The pin–to–pin discharge benchmark settings are derived from [34] because its configuration provides a well–documented discharge setup and operating conditions that can be reproduced numerically and used for comparing different spark models. The details of the model settings are listed in table 3, and the geometry and geometrically refined meshes for the hyperbola electrode curve are shown in figure 6.

The fixed Cartesian mesh used in the conventional/linear field/ambipolar models includes a locally refined region that fully covers the discharge channel ($r < 1.0$ mm, as shown in figure 6(a)). The minimum cell size is identical to that used in the SI–AMR model ($h_{\min} = 2.0\,\mu$m). The adaptive mesh changes dynamically around the discharge region, as shown in figure 6(b). Therefore, the differences in the results and computational costs can be attributed to the modeling choices rather than to any unfair advantage provided by the smallest mesh size.

The electron collision cross–sections of N_2 and O_2 are obtained from the SIGLO and Phelps databases available in Lxcat [65], respectively. The plasma chemistry set is derived from [49], which reports 16 plasma species including electrons, ions, radicals, excited species, and neutral molecules.

Figure 7 shows the spatiotemporal evolution of the electron density and electric field distributions at the sequential discharge stages (4, 6, 8, and 10 ns). The positive and negative streamers propagate from the two electrodes and merge at 4 ns, indicating the onset of plasma channel formation. During the 4–6 ns interval, the spark plasma undergoes lateral expansion, while its electron density increases rapidly (up to $10^{22}\,\mathrm{m}^{-3}$), prompting the SI–AMR framework to switch to the linear electric field model at 6 ns. The 6–10 ns interval is categorized as the spark–discharge stage, during which 'side flares,' due to the implementation of the linear electric field model, are also observed in the *PASSKEy* code. The electron density and electric field distributions obtained using the *PASSKEy* code simulations are consistent with those reported in the reference paper [34].

Figure 8 illustrates the fluid dynamic responses of the spark discharge at 400 and 800 ns. The result agrees with the mass density, pressure, temperature, and velocity reported in the literature. A comparative analysis of the plasma and hydrodynamic responses demonstrates the successful validation of the updated *PASSKEy* code. This updated code employs the SI–AMR framework for streamer discharge

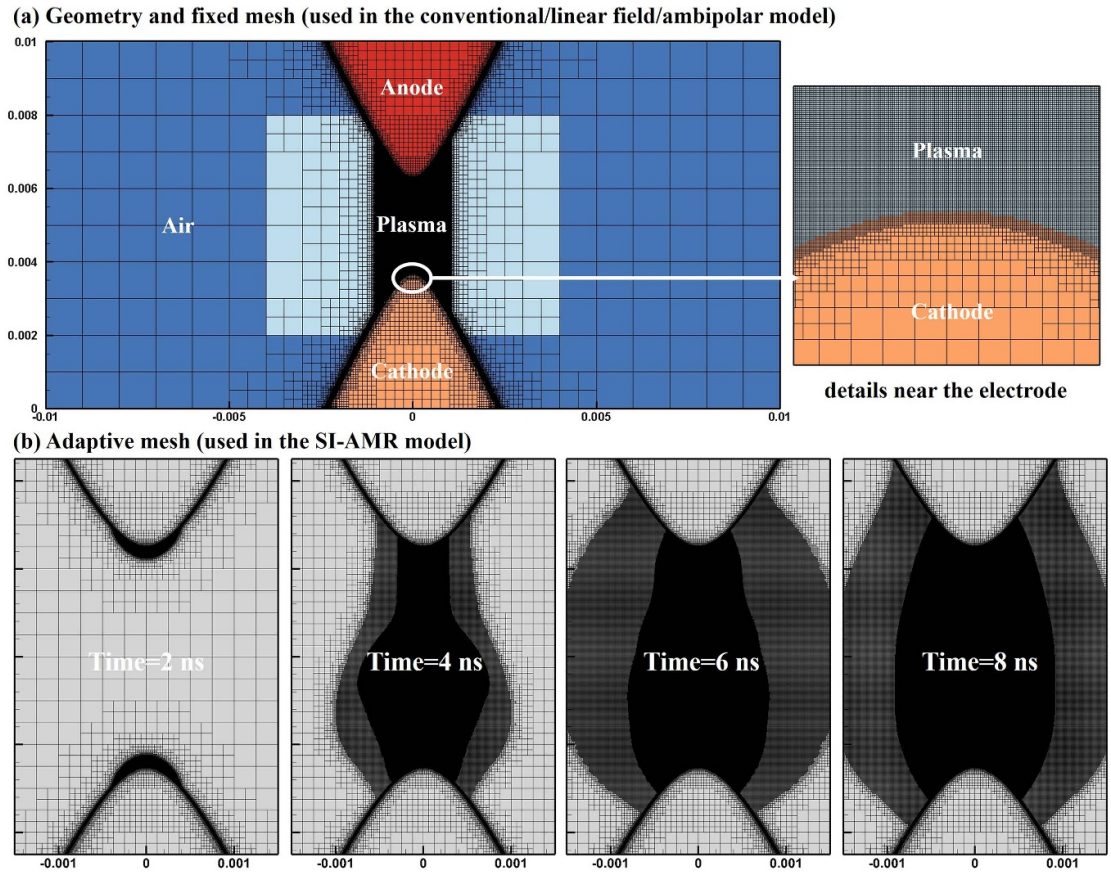

Figure 6. Schematic of (a) 2D axisymmetric geometry and fixed mesh for the conventional/linear field/ambipolar models. (b) AMR for the SI–AMR model (unit in (m)).

computation, coupled with a linear field model for simulating spark discharge in a pin–to–pin discharge benchmark configuration.

According to the calculation results, the 10–ns discharge process can be divided into three stages:

(1) Streamer propagation (0 ns–4 ns): In this duration, the discharge is initiated, and the streamer propagates, with the positive and negative streamers contacting each other at 4 ns (figure 9). Evidently, the spatial E/N and n_e calculated using implicit time integration are consistent with those computed using explicit time integration, demonstrating the validity of the SI–AMR model in streamer discharge modeling. During the streamer propagation, the maximum E/N exceeds 1000 Td, and the maximum n_e is approximately $10^{20}\,m^{-3}$.

(2) Spark growth (4 ns–6 ns): With the merging of positive and negative streamers, the E/N head, which is characterized by a large spatial gradient, gradually diminishes. A discharge channel forms when a voltage of 5100 V is maintained. Subsequently, a spark occurs, resulting in n_e maximizing to $10^{22}\,m^{-3}$ at 5.93 ns, which satisfies the criteria for switching to spark models.

Figure 10 shows the spatial distributions of E/N and n_e at 6 ns; at this instance, only the ambipolar model shows significant differences. The primary difference is the sudden change in E/N accompanied by a small spark diameter. Given the continuous evolution of the voltage profile in the model, E/N should exhibit temporal continuity without abrupt transitions. The discrepancy observed at 6 ns suggests that the ambipolar diffusion approximation is inadequate for modeling the incipient spark. Our analysis reveals a critical limitation in the initial spark phase: an n_e of $10^{21}\,m^{-3}$–$10^{22}\,m^{-3}$ is inadequate for providing sufficient space charge in the early stage of the spark, and thus, this condition violates the fundamental premise of the Laplace field approximation.

(3) Spark maintenance (6 ns–10 ns): During this period, the discharge channel expands radially, and n_e inside the channel increases from approximately $10^{22}\,m^{-3}$ to $10^{23}\,m^{-3}$. Notably, significant differences in the spark morphology are observed among the various spark models.

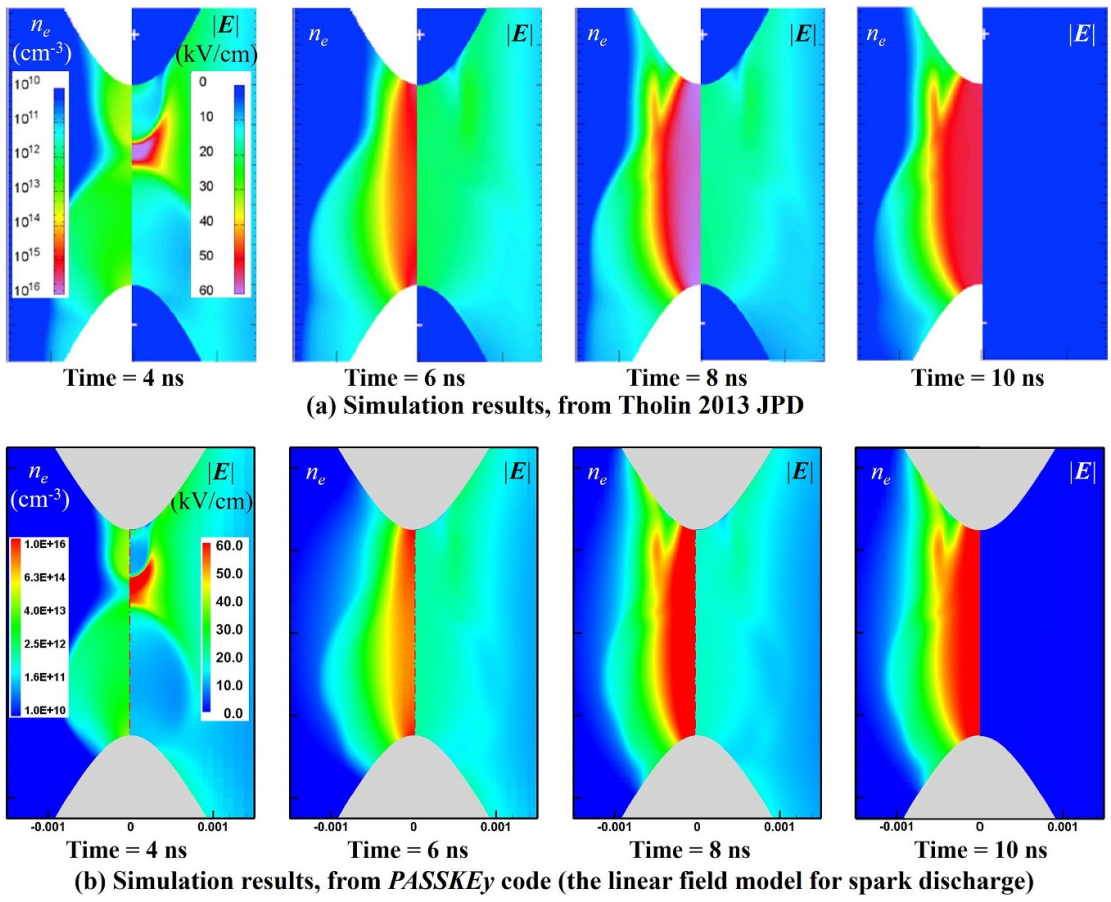

Figure 7. Comparison of the electron density and electric field extracted from (a) [34] with those derived using the (b) *PASSKEy* code. The values are compared at 4, 6, 8, and 10 ns. (a) Reproduced from [34]. © IOP Publishing Ltd. All rights reserved.

If the dielectric relaxation time is reduced to 10^{-15} s, then the conventional explicit plasma–fluid model requires approximately 10 h to simulate a 0.1–ns discharge. This results in computational costs that are approximately 100 times higher than those incurred by other spark modeling models. This exceedingly low computational efficiency renders long–term discharge simulations infeasible on our computational platform. The corresponding results at 8 ns, presented in figure 11(a) are calculated in approximately 2 weeks.

The characteristic 'side flares' phenomenon emerges exclusively in simulations employing the linear field model, as shown in figure 11(b). The conventional explicit, SI–AMR, and linear field models exhibit comparable n_e and E/N distributions at the discharge initiation instant (6 ns). However, notably, the high–field region (exceeding 300 Td) is 'frozen' exclusively in the linear field model. This non–self–consistent field ultimately triggers the formation of 'side flares' at 8 ns. Furthermore, transport fluxes are neglected in the linear model; that is, plasma dynamics are artificially decoupled from the field evolution, thereby intensifying the coupling between the electric field and density distributions. The results obtained in the present study demonstrate that 'side flares' are an inherent drawback of the linear field model. A similar phenomenon has been investigated by Chen *et al* [37] in a pin–plane discharge using the linear electric field model; they have reported the generation of 'side flares' on the surface of an electrode with a small curvature radius.

Notably, the spatial distributions of E/N and n_e in both the ambipolar diffusion and the SI–AMR models remain consistent in the spark maintenance stage, particularly within the plasma channel. This observation confirms the validity of the ambipolar diffusion model in high–density conditions.

The computational times required for modeling four sparks in this study are summarized in table 4. The runtime is recorded by a clock on a desk workstation equipped with an AMD 7950x CPU (16 physical cores, 32 threads) and 64 GB DDR5 RAM. The characteristics of the four spark models used in this study are summarized in table 5.

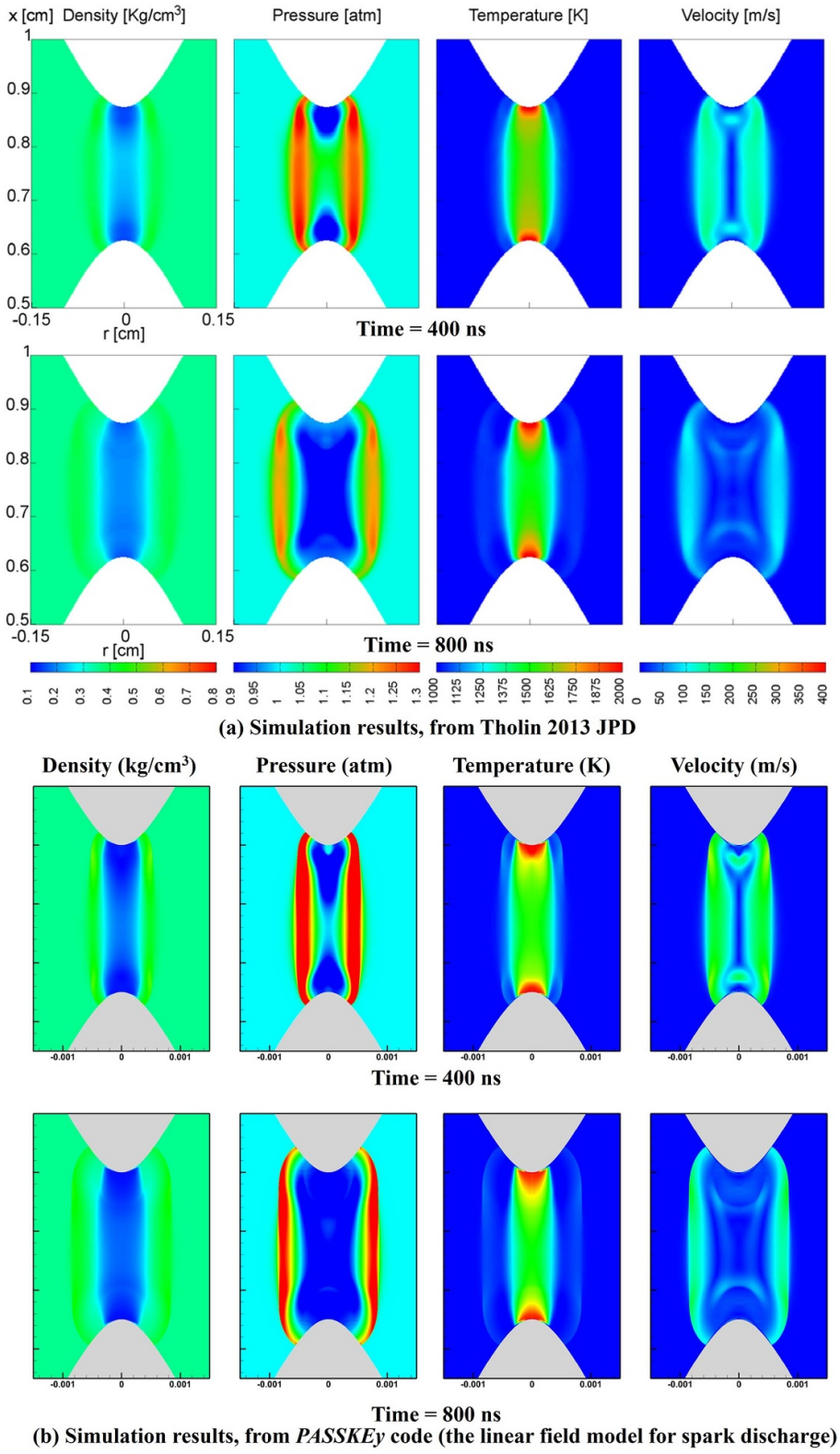

Figure 8. Comparison of fluid dynamic responses (mass density, pressure, temperature, and velocity) extracted from (a) [34] with those derived using the (b) *PASSKEy* code. The values are compared at 400 and 800 ns. Reproduced from (a) [34].

4.2. Error estimation and optimal time steps

The quantitative results obtained from the four spark–discharge models are systematically evaluated and compared to assess their accuracy. The conventional explicit plasma–fluid model is used as the benchmark, and the relative errors of the other three models are computed accordingly. In addition, for

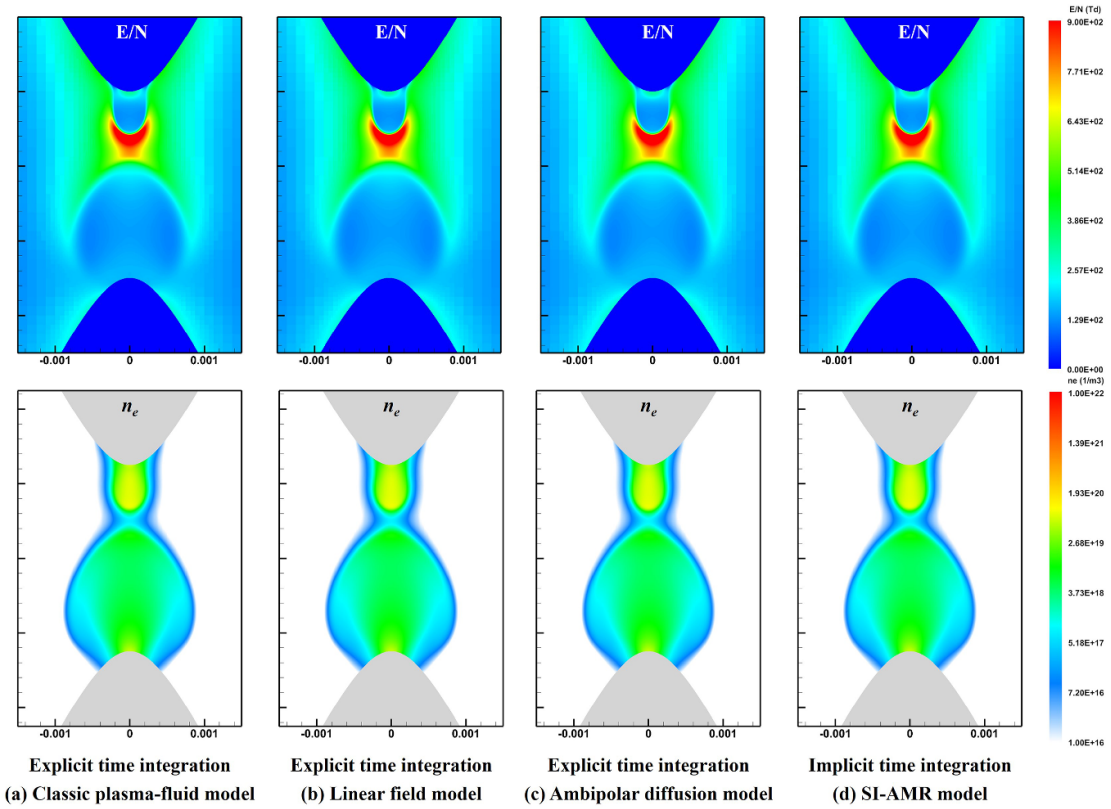

Figure 9. Comparison of spatial *E*/*N* and n_e at 4 ns. (a) Conventional explicit plasma–fluid model, (b) linear field model, (c) ambipolar diffusion model, and (d) SI–AMR model.

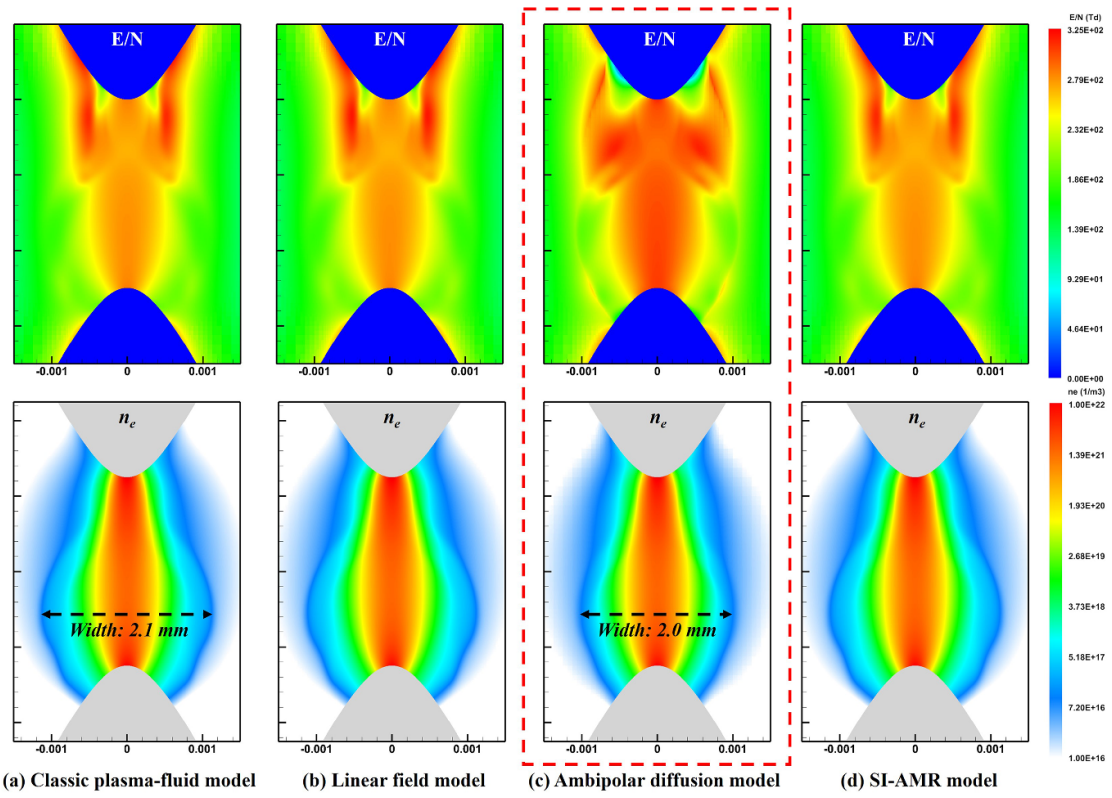

Figure 10. Comparison of spatial *E*/*N* and n_e at 6 ns. (a) Conventional explicit plasma–fluid model, (b) linear field model, (c) ambipolar diffusion model, and (d) SI–AMR model. The red–dashed box marks anomalous results obtained using the ambipolar diffusion model.

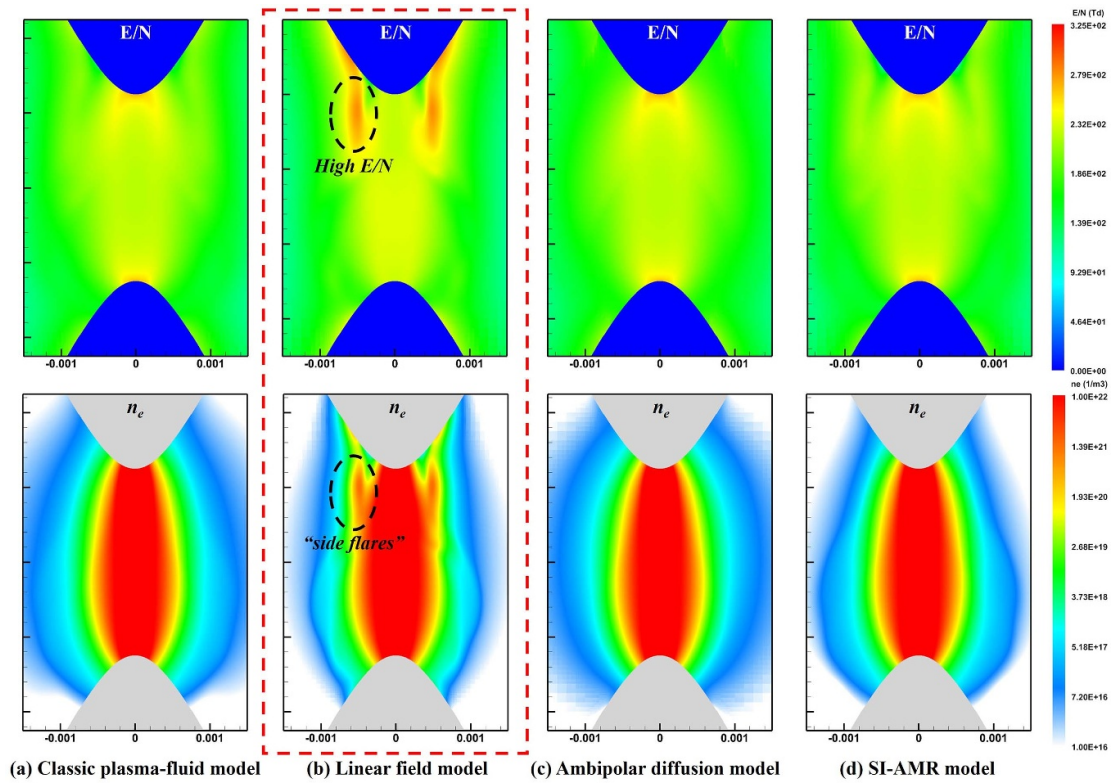

Figure 11. Comparison of spatial E/N and n_e at 8 ns. (a) Conventional explicit plasma–fluid model, (b) linear field model, (c) ambipolar diffusion model, and (d) SI–AMR model. The red–dashed box marks anomalous results obtained using the linear field model.

Table 4. Computational costs of the four models.

Model	Streamer and Spark growth time costs	Spark maintenance time costs	Total time costs
Conventional explicit plasma–fluid model	17.11 h	∼2 weeks	∼2 weeks
Linear field model	17.11 h	7.73 h	24.84 h
Ambipolar diffusion model	17.11 h	4.42 h	21.53 h
SI–AMR model	5.30 h	7.23 h	12.53 h

Table 5. Characteristics of the spark–discharge models.

Model	Features
Conventional explicit plasma–fluid model	High accuracy but extremely low computational efficiency (Limited by the dielectric relaxation time)
Linear field model	Only high accuracy at early spark (Electric fields error increased over time, and may produce nonphysical 'side–flares')
Ambipolar diffusion model	Only high accuracy at late spark (Electric fields mutation happened at model switching)
SI–AMR model	High accuracy and no need to switch the model

the SI–AMR model, the computational efficiency and relative errors are further investigated when different CFL numbers are employed in the spark stage.

(1) Error estimation for the four spark models

The electrode conduction currents are analyzed to quantify the boundary–related discrepancies, as these currents directly reflect the coupled variations in the electric field and density of the charge species.

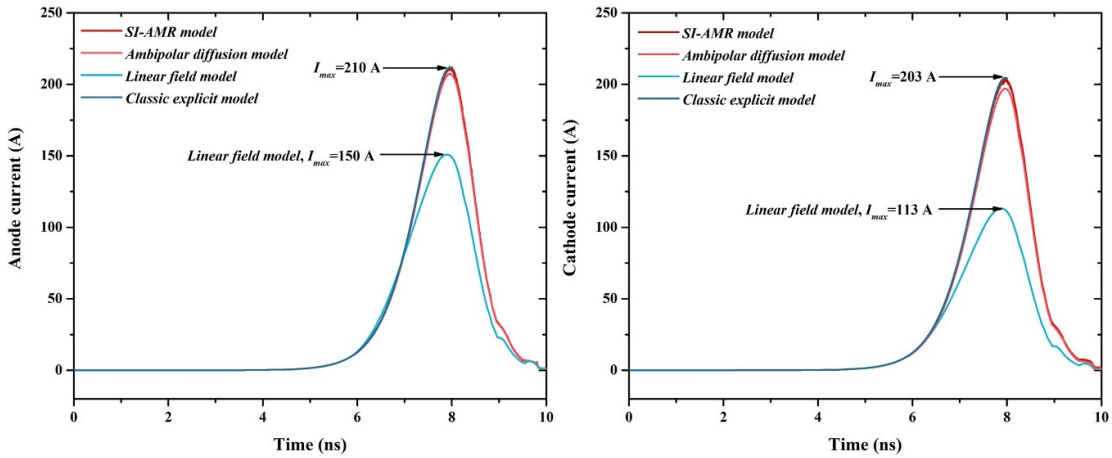

Figure 12. Cathode and anode current profiles in different spark models. The dark–red, light–red, light–blue, and dark–blue lines represent the results obtained using the SI–AMR, ambipolar diffusion, linear field, and conventional explicit models, respectively.

Figure 12 shows the electrode currents for the four spark models. The electrode conduction current is evaluated as

$$I_{\mathrm{c}} = \int_{S} \mathbf{j}_{\mathrm{c}} \cdot \mathrm{d}\mathbf{S}, \tag{38}$$

$$\mathbf{j}_{\mathrm{c}} = e \sum_{i=1}^{N} \mathrm{sgn}\,(q_i)\, \mu_i n_i \mathbf{E}, \tag{39}$$

where I_{c} is the conduction current, j_{c} is the current density, and S is the area of the electrode.

When the conventional explicit plasma–fluid model, without any time acceleration scheme, is used as the benchmark, the SI–AMR model exhibits the lowest relative error, whereas the ambipolar diffusion model yields a relative error of approximately 5%. In contrast, the peak currents at the cathode and anode in the linear field model are approximately 113 and 150 A, respectively, corresponding to relative errors of up to 44.3% and 28.6%, respectively.

Evidently, the linear field model yields markedly low peak currents. This behavior can be attributed to the switch time in the linear field model. When the linear field model is turned on the condition of $n_{\mathrm{e}} > 10^{22}\,\mathrm{m}^{-3}$, we predict that the electric field becomes 'frozen' prematurely. As a result, the electric field remains insufficiently uniform and its magnitude deviates noticeably from the benchmark solution, which leads to underestimated results in subsequent calculations. Besides, The electron densities and E/N values, in the vicinity of both the electrodes, predicted by the linear field model are lower than those determined using the other three models. Figure 13 displays the axial profiles of the electron density and reduced electric field E/N, at 8 ns, predicted by the four models (conventional explicit, linear field, ambipolar diffusion, and SI–AMR models). These low values reduce the local conductivity and thus decrease the surface current density, leading to substantially low peak electrode currents.

To verify this interpretation, we delay the activation time of the linear field model and examine how the predicted current responds to the switching time. By delaying the activation of the linear field model (figure 14), we observe that the later the linear field model is switched on, the closer the predicted current amplitude approaches that obtained with the other three spark–discharge models.

Figure 15 presents the radial profiles extracted at 8 ns on the mid–plane ($z = 0$ mm), providing additional insights into the spatial discrepancies among the four spark–discharge models. Overall, the four models predict consistent values of the electron density ($n_{\mathrm{e}}(r)$) prevalent in the core of the discharge channel. However, at distances away from the axis, the linear field model shows noticeably large deviations in the electron density, indicating a less accurate description of plasma spreading near the channel periphery. The reduced field $E/N(r)$ exhibits more pronounced differences; that is, the value predicted by the linear field model deviates significantly across the entire radial range, whereas that predicted by the ambipolar diffusion model shows reasonably good agreement with the benchmark in the late spark stage.

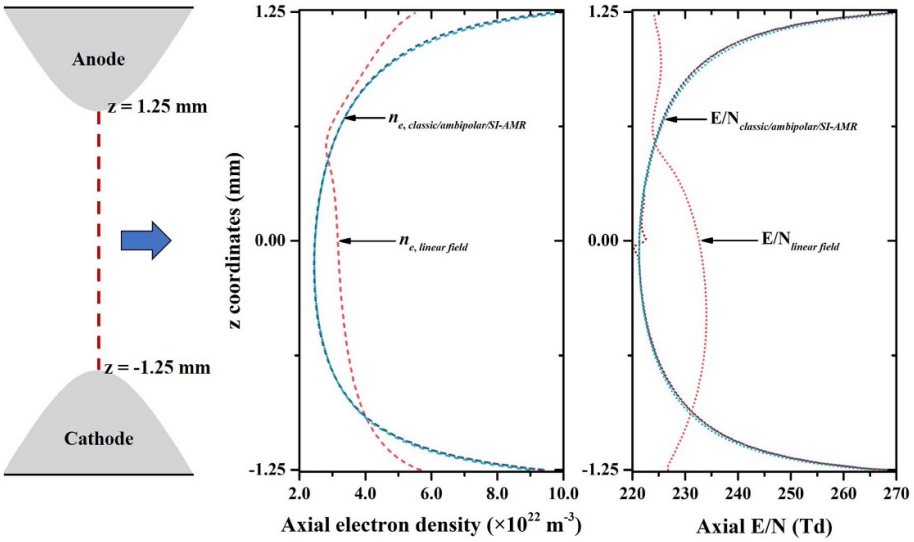

Figure 13. Axial centerline profiles of electron density and reduced electric field at 8 ns, predicted by the four spark models (conventional explicit, linear field, ambipolar diffusion, and SI–AMR models).

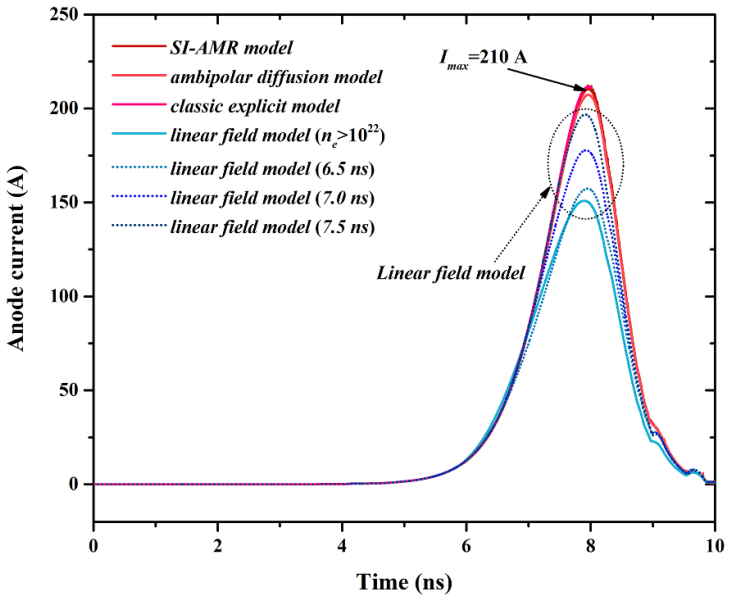

Figure 14. Anode current profiles, the short dotted lines denote cases in which the linear field model is activated at 6.5, 7.0, and 7.5 ns, respectively.

Conversely, the values predicted by the SI–AMR model show the best agreement with the benchmark across the full radial extent, suggesting that this model maintains a low spatial error while improving the computational efficiency.

(2) Optimal time steps of the AMR model

The SI time integration method for transport fluxes can alleviate the CFL constraints. However, it cannot accurately capture discontinuities such as shock waves in computational fluid dynamics and streamer heads in plasma simulations. Therefore, a variable CFL setting is implemented in the SI–AMR model. For streamer and early spark discharges ($n_{e,max} \leqslant 10^{22}$ m^{-3}), we set the CFL number to 0.1 to accurately resolve the steep ionization wavefront. During the spark maintenance stage ($n_{e,max} \geqslant 10^{22}$ m^{-3}), we employ a variable CFL setting, ranging from 0.1 to 10.0, to evaluate both the acceleration efficiency and relative errors.

Figure 16 summarizes the computational time costs of the SI–AMR simulations for the different CFL numbers used in the spark stage. The total runtime is decomposed into streamer–stage runtime (blue) and spark–stage runtime (hatched). Increasing the spark–stage CFL markedly reduces the additional

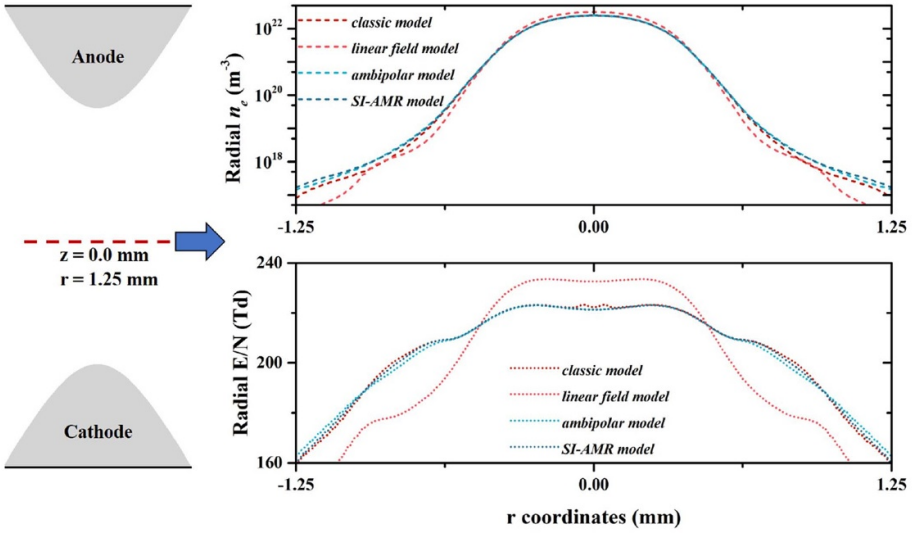

Figure 15. Radial profiles of electron density and reduced electric field at 8 ns on the mid–plane ($z = 0$ mm) predicted by the four spark–discharge models (classic, linear field, ambipolar, and SI–AMR models).

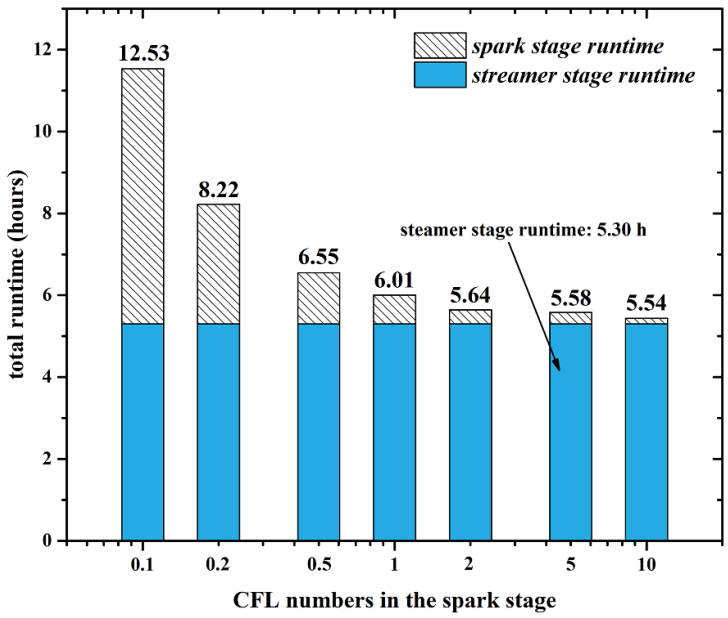

Figure 16. Total runtime for different CFL numbers in the spark stage, and all the cases are calculated using the SI–AMR version of *PASSKEy* code. The stacked bars show the runtimes of the streamer stage (blue; 5.30 (h) and spark stage (hatched); the numbers above the bars indicate total runtimes.

cost in the high–electron–density regime. Evidently, the spark–stage runtime decreases from 7.32 h at a CFL number of 0.1 to 0.14 h at a CFL number of 10.0; consequently, the total runtime decreases from 12.53 h to 5.54 h. In contrast, the streamer–stage runtime remains approximately constant (approximately 5.30 h) because the streamer evolution is always accompanied by a fixed CFL number, thus accurately resolving the steep ionization front. Therefore, once the spark–stage cost is sufficiently reduced (typically for CFL>1), further increasing the CFL number yields diminishing returns, because the total runtime becomes increasingly bounded by the fixed streamer–stage cost.

Figure 17 compares the cathode and anode current waveforms obtained with different CFL numbers in the spark stage of the SI–AMR simulations. For CFL values between 0.1 and 5.0, the current traces nearly overlap over the entire discharge duration, and the peak currents at the cathode and anode are approximately 200 and 210 A, respectively. This result indicates that maintaining moderate CFL values is essential for accurately predicting the electrode current. In contrast, when the CFL number is increased to 10.0, significant oscillations appear during the rapid rise of the current and near the peak

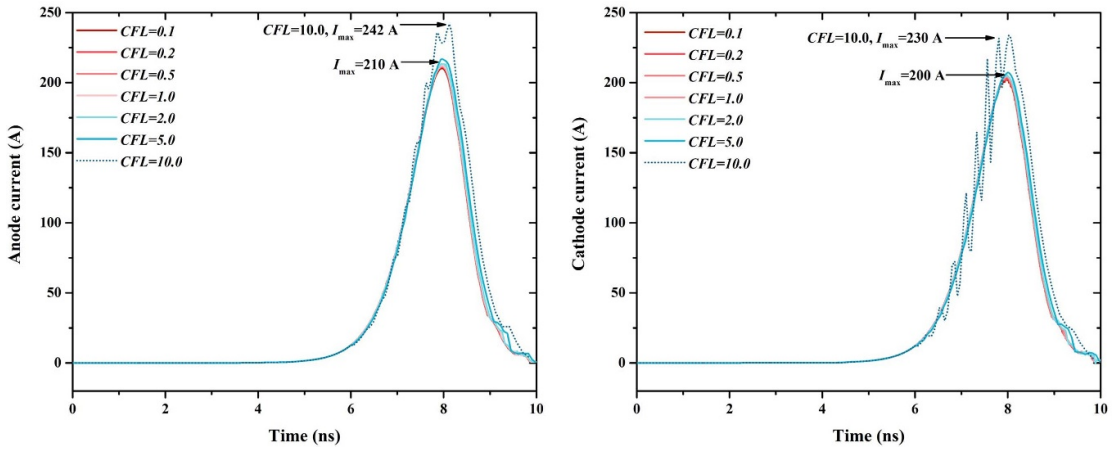

Figure 17. Cathode and anode current profiles obtained with different spark–stage CFL numbers (0.1–10.0) using the SI–AMR model. For CFL numbers of 0.1–5.0, the peak currents remain close to the reference values, whereas for a CFL number of 10.0, pronounced current oscillations and a large relative error are observed.

(approximately 7–8 ns), resulting in overestimated peak currents of approximately 230 and 242 A at the cathode and anode, respectively. These current values are approximately 15% deviated from that observed in the reference case, demonstrating that an excessively large CFL number in the spark stage can compromise the temporal accuracy and introduce an oscillatory current.

Figure 18(a) illustrates the axial profiles of the electron density and E/N, revealing the relative errors within the discharge channel. Cases with CFL numbers between 0.1 and 5.0 exhibit negligible errors in the axial electron–density distributions, whereas the configuration with a CFL number of 10.0 shows significant deviations and oscillatory artifacts. The discrepancies in E/N are even more pronounced; noticeable deviations in the axial electric field already emerge at a CFL number of 5.0. The middle–radial profiles of the electron density and E/N (figure 18(b)) exhibit similar trends. Although the error in the radial electron density is minimal, the error in E/N exceeds 5% at CFL numbers of 5.0 and over 15% at CFL = 10.0, respectively.

Based on these findings, we recommend adopting a CFL value of 2.0 for spark–discharge simulations to achieve an optimal balance between computational efficiency and accuracy preservation.

5. Conclusions

In this study, we comprehensively analyzed various spark–discharge models, developed a unified simulation framework (SI–AMR model) for streamer–spark discharges within the *PASSKEy* code, and optimized the time–step range while estimating the associated errors. The key conclusions drawn from the findings of our study are as follows:

(1) Our systematic evaluation of the conventional explicit plasma–fluid, linear field, and ambipolar diffusion models revealed several deficiencies. The conventional explicit fluid model is comprehensive, but exhibits extreme computational inefficiency, requiring approximately 10 h to simulate a 0.1–ns discharge owing to a dielectric relaxation time of the order of 10^{-15} s; thus, its computational speed was approximately 100 times lower than that of the alternative approaches. The linear field model, although computationally faster, exhibited significant errors; for instance, the relative errors in the electrode currents reached up to 44.3% at the cathode and 28.6% at the anode, and it introduced artificial phenomena such as ‘side flares’ due to its non–self–consistent treatment of the electric field. The ambipolar diffusion model showed intermediate performance; however, it could not capture incipient spark phases effectively, thus showing limited applicability in high–density conditions.

(2) By integrating AMR and SI time integration into the *PASSKEy* code, we established a unified framework for simulating the entire streamer–spark discharge process without requiring model switching. This SI–AMR model successfully captured both the fast dynamics of streamer propagation and the complex evolution of spark discharges. The framework demonstrated excellent agreement with experimental data and those obtained using the conventional explicit fluid model, while significantly reducing the computational time. For example, the simulation time decreased

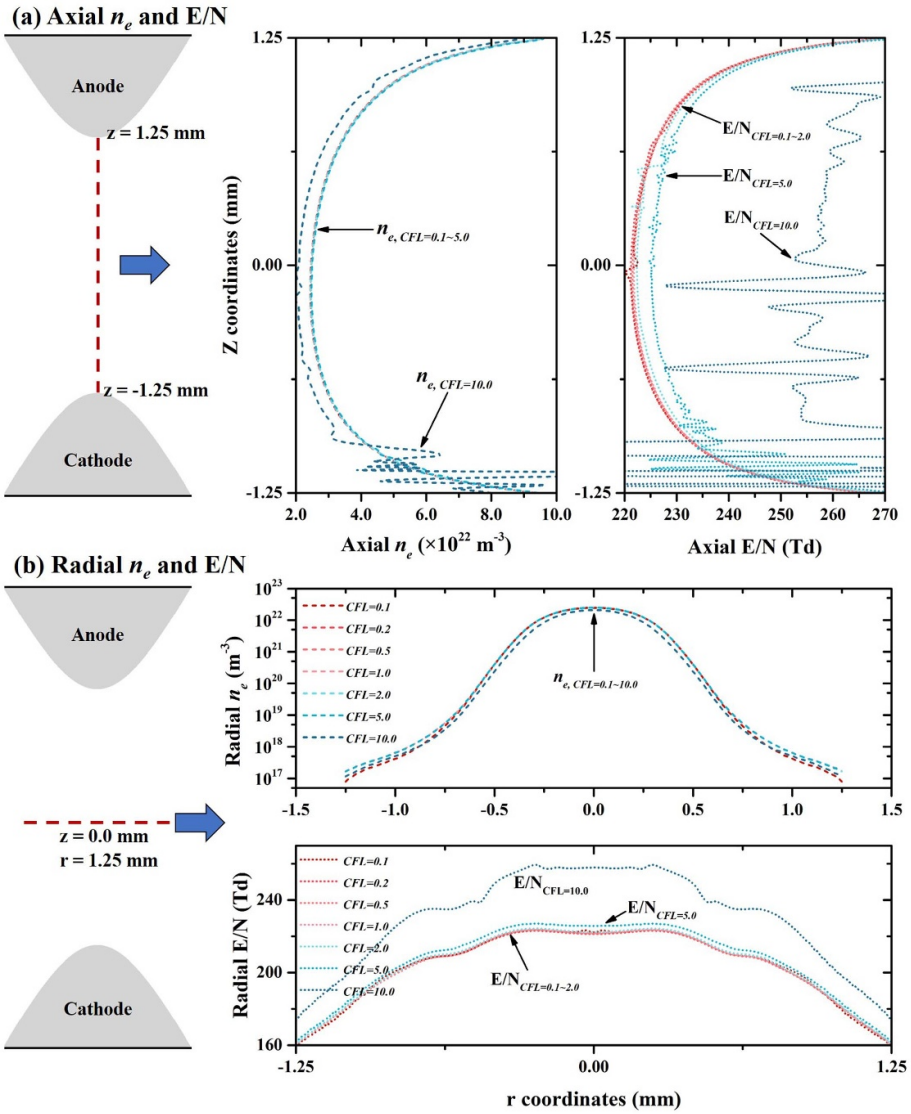

Figure 18. (a) Axial profiles of electron density n_e and E/N, and (b) mid–radial profiles of n_e and E/N. Comparison results for different spark–stage CFL numbers (0.1–10.0) in the SI–AMR model. Cases with CFL = 0.1–5.0 show small deviations in n_e, whereas E/N becomes noticeably more sensitive (deviations emerging at CFL = 5.0); CFL = 10.0 exhibits significant deviations and oscillatory artifacts.

from 7.32 h at a CFL value of 0.1 to 0.14 h at a CFL of 10.0, even though acceleration gains tapered off beyond the CFL number of 1.0 for fixed streamer discharge durations.

(3) A variable CFL setting was implemented to balance computational efficiency and accuracy. During the streamer and early spark phases, a low CFL number (0.1) was employed to accurately resolve the steep ionization fronts. In contrast, during the spark maintenance phase, the CFL number was varied between 0.1 and 10.0. A detailed error analysis showed that while the relative errors in the electrode current remained below 5% for CFL numbers between 0.1 and 5.0, they exceeded 15% at a CFL number of 10.0. Consequently, a CFL number of 2.0 is recommended, as it achieves an optimal balance between computational time reduction and the preservation of simulation accuracy. This conclusion is supported by comparisons of the axial and radial profiles of the electron density, electric field, and overall discharge current measurements.

Acknowledgments

The work is supported by the National Natural Science Foundation Basic Science Center Project (52488101), National Natural Science Foundation of China (No. 52025064, 52277168, 92271113, U2341277, 52107174). The authors thank the young research group in Atelier des Plasmas for fruitful discussions and the Gongfang Tech Co, Ltd for technical support.

Data availability statement

All data that support the findings of this study are included within the article (and any supplementary files).

ORCID iDs

Xiaochi Ma 0000-0003-0951-9338
Luying Bai 0009-0006-4758-4770
Yifei Zhu 0000-0001-8989-0051
Yun Wu 0000-0002-8575-0665

References

[1] Lu P, Boehm D, Bourke P and Cullen P J 2017 Achieving reactive species specificity within plasma-activated water through selective generation using air spark and glow discharges *Plasma Process. Polym.* **14** 1600207
[2] Tachibana K and Nakamura T 2019 Comparative study of discharge schemes for production rates and ratios of reactive oxygen and nitrogen species in plasma activated water *J. Phys. D: Appl. Phys.* **52** 385202
[3] Pareek P, Kooshki S, Tóth P and Janda M 2024 Tuning composition of plasma activated water generated by transient spark discharge with electrospray *Chem. Eng. J.* **493** 152583
[4] Li S, Medrano J A, Hessel V and Gallucci F 2018 Recent progress of plasma-assisted nitrogen fixation research: a review *Processes* **6** 248
[5] Chen H, Yuan D, Wu A, Lin X and Li X 2021 Review of low-temperature plasma nitrogen fixation technology *Waste Disposal Sustain. Energy* **3** 201–17
[6] Zhang S, Zong L, Zeng X, Zhou R, Liu Y, Zhang C, Pan J, Cullen P J, Ostrikov K K and Shao T 2022 Sustainable nitrogen fixation with nanosecond pulsed spark discharges: insights into free-radical-chain reactions *Green Chem.* **24** 1534–44
[7] Li Y, Luo Y, Man C, Pei X, Lu X and Graves D B 2024 Enhancing nitrogen fixation efficiency in glow-like discharge by reducing cathode-fall voltage *Plasma Sources Sci. Technol.* **33** 105014
[8] Pancheshnyi S, Eismann B, Hagelaar G and Pitchford L 2008 Computer code zdplaskin *University of Toulouse, Laplace* (CNRS-UPS-INP)
[9] Lietz A M and Kushner M J 2016 Air plasma treatment of liquid covered tissue: long timescale chemistry *J. Phys. D: Appl. Phys.* **49** 425204
[10] Teunissen J and Ebert U 2016 3D PIC-MCC simulations of discharge inception around a sharp anode in nitrogen/oxygen mixtures *Plasma Sources Sci. Technol.* **25** 044005
[11] Kushner M J 2004 Modeling of microdischarge devices: pyramidal structures *J. Appl. Phys.* **95** 846–59
[12] Breden D, Miki K and Raja L 2012 Self-consistent two-dimensional modeling of cold atmospheric-pressure plasma jets/bullets *Plasma Sources Sci. Technol.* **21** 034011
[13] Bourdon A, Bonaventura Z and Celestin S 2010 Influence of the pre-ionization background and simulation of the optical emission of a streamer discharge in preheated air at atmospheric pressure between two point electrodes *Plasma Sources Sci. Technol.* **19** 034012
[14] Tholin F, Lacoste D A and Bourdon A 2014 Influence of fast-heating processes and O atom production by a nanosecond spark discharge on the ignition of a lean H2–air premixed flame *Combust. Flame* **161** 1235–46
[15] Zhang B, Zhu Y, Zhang X, Popov N, Orrière T, Pai D Z and Starikovskaia S M 2023 Streamer-to-filament transition in pulsed nanosecond atmospheric pressure discharge: 2D numerical modeling *Plasma Sources Sci. Technol.* **32** 115014
[16] Unfer T, Boeuf J-P, Rogier F and Thivet F 2010 Multi-scale gas discharge simulations using asynchronous adaptive mesh refinement *Comput. Phys. Commun.* **181** 247–58
[17] Teunissen J and Ebert U 2018 Afivo: a framework for quadtree/octree AMR with shared-memory parallelization and geometric multigrid methods *Comput. Phys. Commun.* **233** 156–66
[18] Pancheshnyi S, Ségur P, Capeillère J and Bourdon A 2008 Numerical simulation of filamentary discharges with parallel adaptive mesh refinement *J. Comput. Phys.* **227** 6574–90
[19] Liu N 2025 Adaptive modeling of plasma initiation, filamentation and interaction *J. Comput. Phys.* **530** 113887
[20] Niknezhad M, Chanrion O, Holbøll J and Neubert T 2021 Dynamics of negative coronas in airflow *Plasma Sources Sci. Technol.* **30** 105001
[21] Lin B, Zhuang C, Cai Z, Zeng R and Bao W 2020 An efficient and accurate MPI-based parallel simulator for streamer discharges in three dimensions *J. Comput. Phys.* **401** 109026
[22] Teunissen J and Ebert U 2017 Simulating streamer discharges in 3D with the parallel adaptive afivo framework *J. Phys. D: Appl. Phys.* **50** 474001
[23] Lin B, Zhuang C and Shi Q 2024 Adaptive mesh refinement and embedded boundary method for streamer discharge simulations *IEEE Trans. Magn.* **60** 1–4
[24] Montijn C, Hundsdorfer W and Ebert U 2006 An adaptive grid refinement strategy for the simulation of negative streamers *J. Comput. Phys.* **219** 801–35
[25] Unfer T and Boeuf J-P 2009 Modelling of a nanosecond surface discharge actuator *J. Phys. D: Appl. Phys.* **42** 194017
[26] Kolobov V and Arslanbekov R 2012 Towards adaptive kinetic-fluid simulations of weakly ionized plasmas *J. Comput. Phys.* **231** 839–69
[27] Unfer T 2013 An asynchronous framework for the simulation of the plasma/flow interaction *J. Comput. Phys.* **236** 229–46
[28] Korkut B, Li Z and Levin D A 2015 3-D simulation of ion thruster plumes using octree adaptive mesh refinement *IEEE Trans. Plasma Sci.* **43** 1706–21
[29] Niknezhad M, Chanrion O, Köhn C, Holbøll J and Neubert T 2021 A three-dimensional model of streamer discharges in unsteady airflow *Plasma Sources Sci. Technol.* **30** 045012

[30] Papadakis A, Georghiou G E and Metaxas A 2008 New high quality adaptive mesh generator utilized in modelling plasma streamer propagation at atmospheric pressures *J. Phys. D: Appl. Phys.* **41** 234019
[31] Benkhaldoun F, Fořt J, Hassouni K and Karel J 2012 Simulation of planar ionization wave front propagation on an unstructured adaptive grid *J. Comput. Appl. Math.* **236** 4623–34
[32] Kissami I, Maazioui S and Benkhaldoun F 2022 Parallel finite volume code for plasma with unstructured adaptive mesh refinement *The 8th European Cong. on Computational Methods in Applied Sciences and Engineering*
[33] Khomich V, Shershunova E, Shakhmatov E, Voevodin V, Yamshchikov V and Zharkov Y 2025 Numerical model of streamer discharge with adaptive mesh and KKT-based mass correction *J. Phys. D: Appl. Phys.* **58** 485202
[34] Tholin F and Bourdon A 2013 Simulation of the hydrodynamic expansion following a nanosecond pulsed spark discharge in air at atmospheric pressure *J. Phys. D: Appl. Phys.* **46** 365205
[35] Tarasenko V, Naidis G, Beloplotov D, Kostyrya I and Babaeva N Y 2018 Formation of wide streamers during a subnanosecond discharge in atmospheric-pressure air *Plasma Phys. Rep.* **44** 746–53
[36] Guo Y, Zhang Y, Zhu Y, Jeanney P, Brisset A, Sun A and Tardiveau P 2025 Numerical investigation of atmospheric positive diffuse discharge mode transition: the effect of voltage rise time *J. Phys. D: Appl. Phys.* **58** 445205
[37] Chen X, Zhu Y and Wu Y 2020 Modeling of streamer-to-spark transitions in the first pulse and the post discharge stage *Plasma Sources Sci. Technol.* **29** 095006
[38] Raizer Y P and Allen J E 1997 *Gas Discharge Physics* vol 2 (Springer)
[39] Kolev S and Bogaerts A 2014 A 2D model for a gliding arc discharge *Plasma Sources Sci. Technol.* **24** 015025
[40] Sun S, Kolev S, Wang H and Bogaerts A 2016 Coupled gas flow-plasma model for a gliding arc: investigations of the back-breakdown phenomenon and its effect on the gliding arc characteristics *Plasma Sources Sci. Technol.* **26** 015003
[41] Sun S, Kolev S, Wang H and Bogaerts A 2017 Investigations of discharge and post-discharge in a gliding arc: a 3D computational study *Plasma Sources Sci. Technol.* **26** 055017
[42] Ventzek P L, Sommerer T J, Hoekstra R J and Kushner M J 1993 Two-dimensional hybrid model of inductively coupled plasma sources for etching *Appl. Phys. Lett.* **63** 605–7
[43] Kushner M J 2009 Hybrid modelling of low temperature plasmas for fundamental investigations and equipment design *J. Phys. D: Appl. Phys.* **42** 194013
[44] Villa A, Barbieri L, Gondola M, Leon-Garzon A R and Malgesini R 2014 Mesh dependent stability of discretization of the streamer equations for very high electric fields *Comput. Fluids* **105** 1–7
[45] Lin K-M, Hung C-T, Hwang F-N, Smith M R, Yang Y-W and Wu J-S 2012 Development of a parallel semi-implicit two-dimensional plasma fluid modeling code using finite-volume method *Comput. Phys. Commun.* **183** 1225–36
[46] Li J-Z, Zhao M-L, Zhang Y-R, Gao F and Wang Y-N 2025 Fast simulation strategy for capacitively-coupled plasmas based on fluid model *Comput. Phys. Commun.* **307** 109392
[47] Dung N T, Besse C and Rogier F 2024 An implicit time integration approach for simulation of corona discharges *Comput. Phys. Commun.* **294** 108906
[48] Zhu Y, Shcherbanev S, Baron B and Starikovskaia S 2017 Nanosecond surface dielectric barrier discharge in atmospheric pressure air: I. Measurements and 2D modeling of morphology, propagation and hydrodynamic perturbations *Plasma Sources Sci. Technol.* **26** 125004
[49] Zhu Y and Starikovskaia S 2018 Fast gas heating of nanosecond pulsed surface dielectric barrier discharge: spatial distribution and fractional contribution from kinetics *Plasma Sources Sci. Technol.* **27** 124007
[50] Hagelaar G and Pitchford L C 2005 Solving the Boltzmann equation to obtain electron transport coefficients and rate coefficients for fluid models *Plasma Sources Sci. Technol.* **14** 722
[51] Pancheshnyi S 2014 Photoionization produced by low-current discharges in O2, air, N2 and CO2 *Plasma Sources Sci. Technol.* **24** 015023
[52] Guo Y, Li Y, Zhu Y and Sun A 2023 A numerical and experimental study on positive diffusive ionization waves in different N2/CO2 mixtures: the role of photoionization *Plasma Sources Sci. Technol.* **32** 025003
[53] Zhu Y, Wu Y, and Li J 2020 Photopic: calculate photo-ionization functions and model coefficients for gas discharge simulations (arXiv:2005.10021)
[54] Soloviev V R and Krivtsov V M 2018 Numerical modelling of nanosecond surface dielectric barrier discharge evolution in atmospheric air *Plasma Sources Sci. Technol.* **27** 114001
[55] Célestin S 2008 Study of the dynamics of streamers in air at atmospheric pressure *PhD Thesis* Ecole Centrale Paris
[56] Chen S, Nobelen J and Nijdam S 2017 A self-consistent model of ionic wind generation by negative corona discharges in air with experimental validation *Plasma Sources Sci. Technol.* **26** 095005
[57] Scarcelli R, Biswas S, Ekoto I, Breden D, Karpatne A and Raja L 2018 7.2 numerical simulation of a nano-pulsed high-voltage discharge and impact on low-temperature plasma ignition processes for automotive applications *Ignition Systems for Gasoline Engines: Internationale Tagung ZüNdsysteme für Ottomotoren* p 329
[58] Eichwald O, Ducasse O, Dubois D, Abahazem A, Merbahi N, Benhenni M and Yousfi M 2008 Experimental analysis and modelling of positive streamer in air: towards an estimation of O and N radical production *J. Phys. D: Appl. Phys.* **41** 234002
[59] Celestin S, Bonaventura Z, Zeghondy B, Bourdon A and Ségur P 2009 The use of the ghost fluid method for Poisson's equation to simulate streamer propagation in point-to-plane and point-to-point geometries *J. Phys. D: Appl. Phys.* **42** 065203
[60] Ma X, Bai L, Zhu Y, Jiang X and Wu Y 2024 Numerical investigation of discharge evolution and breakdown characteristics of ArF excimer lasers *Plasma Sources Sci. Technol.* **33** 075012
[61] Blazek J 2015 *Computational Fluid Dynamics: Principles and Applications* (Butterworth-Heinemann)
[62] Kulikovsky A 1995 A more accurate Scharfetter-Gummel algorithm of electron transport for semiconductor and gas discharge simulation *J. Comput. Phys.* **119** 149–55
[63] Pechereau F 2013 Numerical simulation of the interaction of atmospheric pressure plasma discharges with dielectric surfaces *PhD Thesis* Ecole Centrale Paris
[64] Batty C 2017 A cell-centred finite volume method for the poisson problem on non-graded quadtrees with second order accurate gradients *J. Comput. Phys.* **331** 49–72
[65] Pitchford L C *et al* 2017 Lxcat: an open-access, web-based platform for data needed for modeling low temperature plasmas *Plasma Proces. Polym.* **14** 1600098